Role of Turbulent Shear Rate Distribution in Aggregation and Breakage Processes

Daniele L. Marchisio
Dipartimento di Scienza Materiali ed Ingegneria Chimica, Politecnico di Torino, I-10129 Torino, Italy

Miroslav Soos, Jan Sefcik, and Massimo Morbidelli
Institut für Chemie- und Bioingenieurswissenschaften, Swiss Federal Institute of Technology Zürich, ETH Hönggerberg/HCI, CH-8093 Zurich, Switzerland

DOI 10.1002/aic.10614
Published online September 1, 2005 in Wiley InterScience (www.interscience.wiley.com).

The effect of spatial flow heterogeneity on shear-induced aggregation and breakage of fine particles in turbulent flow conditions is investigated using computational fluid dynamics (CFD) and population balance modeling. The quadrature method of moments (QMOM), particularly suitable for implementation in commercial CFD codes, has been used to solve the corresponding population balance equation. QMOM is first tested and compared with alternative numerical methods (sectional/fixed-pivot methods) for a specific set of realistic operating conditions. Then QMOM is implemented in a CFD code and the effect of spatial heterogeneities on the cluster mass distribution in a Taylor–Couette vessel is investigated. Simplified models have been derived based on the separation of the timescales of mixing on one hand and of aggregation and breakage on the other and compared with the full CFD model. Guidelines for use and limitations of such models and the identification of the underlying aggregation and breakage kernels are discussed. © 2005 American Institute of Chemical Engineers *AIChE J,* 52: 158–173, 2006
Keywords: population balance, computational fluid dynamics, aggregation, breakage, quadrature method of moments, classes method, polymer colloids

Introduction

Aggregation and breakage of fine and ultrafine particles in sheared dispersions is a relevant process in chemical engineering. Water treatment, polymer postprocessing, mineral dispersion, and crystallization are a few of numerous applications where aggregation and breakage of particles play an important role. The final products are in the form of a population of aggregates commonly described by a particle or cluster size distribution (PSD). Aggregates often have fractal-like structure, which means that their mass scales with size with an exponent known as fractal dimension,[1] which in turn determines their density and mechanical properties.

Aggregate populations can be characterized by various experimental techniques, including light scattering, sound spectroscopy, or microscopy. Light-scattering methods are widely used to characterize diluted dispersions and they allow one to obtain average properties of the cluster mass distribution (CMD), such as the average radius of gyration or the mass-weighted average mass, as well as information about the aggregate structure through the structure factor. Several studies have used these techniques to monitor aggregation and breakage in dilute colloidal dispersions for various types, sizes, and concentrations of primary particles in various flow conditions.[2-9] The aim of these studies is to quantify the effect of operating conditions on the resulting aggregate properties in terms of their size and structure.

Present address of J. Sefcik: Department of Chemical and Process Engineering, University of Strathclyde, James Weir Building, 75 Montrose Street, Glasgow G1 1XJ, Scond, UK.

From a modeling perspective suitable population balance models have been developed to describe observed trends and to estimate unknown model parameters. In most cases such analysis assumed that the shear rate was homogeneous and was taken equal to the volume-averaged value calculated from the power input of the shearing device. In this case it is relatively straightforward to solve the resulting population balance models to obtain the time evolution of the aggregate size distribution or their moments.[10-14] Although this approach has its own value, if one needs a quantitatively reliable simulation, one must properly account for the detailed hydrodynamic conditions in the vessel, which for this kind of processes play a very important role. The danger, for example, is that the model parameters fitted at a small scale cannot be transferred to a larger scale just because the hydrodynamic conditions are changed.

The main operating parameter that affects the aggregate properties in sheared dispersions is the shear rate (or the turbulent energy dissipation rate in turbulent flows), which controls the rate of collision and therefore the rate of cluster aggregation as well as the rate of breakage. A few previous studies addressed issues of flow heterogeneity by using detailed modeling approaches in either laminar[15] or turbulent conditions[16-19] and showed significant differences compared to simplified models assuming homogeneous distribution of the shear rate. This is in agreement with the experimental results[20-22] obtained using various types of impellers and vessel volumes operated at the same volume-averaged shear rate. Therefore it is important to properly include the spatial distribution of the shear rate in population balance models.

This work investigates the detailed modeling of aggregating systems, with particular attention to the role of spatially heterogeneous shear rate and mixing. First, two different numerical methods are tested to solve the population balance equation (PBE) for fractal aggregates—that is, the classes (pivot) method with various grid choices and the quadrature method of moments (QMOM)—and their performances are compared in terms of accuracy and computational costs. One of them (QMOM) is implemented in a computational fluid dynamics (CFD) code and the effect of flow heterogeneity on the time evolution of the average properties of the CMD, such as the average radius of gyration and the zero-angle intensity, is investigated. Furthermore, simplified models based on the hypothesis of infinitely fast mixing and infinitely fast CMD relaxation are formulated and compared with the full CFD model. The investigations are carried out in turbulent conditions for a Taylor–Couette vessel. The article is organized as follows: first the governing equations are presented, then the fully distributed model and the simplified models are derived and analyzed. Simulation results are presented and analyzed and the discussion is concluded with the proposal of general criteria about applicability of simplified models and their limitations.

Governing Equations

We restrict our study to turbulent systems and we assume that the characteristic rate of aggregation and breakage is slower than that of turbulent fluctuations. In this case the Reynolds average can be easily applied because all the terms appearing in the PBE are uncorrelated. In what follows we present the governing equations of the process under investigation and then we identify four different modeling approaches for accounting for spatial heterogeneities. The PBE written in terms of one internal coordinate,[23] after Reynolds average and after closing the convective transport term by means of turbulent diffusivity, is expressed as follows

$$\frac{\partial n(\xi;\mathbf{x},t)}{\partial t}+\frac{\partial}{\partial x_i}\left[\langle u_i\rangle n(\xi;\mathbf{x},t)\right]-\frac{\partial}{\partial x_i}\left[D_t\frac{\partial n(\xi;\mathbf{x},t)}{\partial x_i}\right]$$
$$=\frac{1}{2}\int_0^{\xi}k^A(G;\xi-\xi',\xi')n(\xi-\xi';\mathbf{x},t)n(\xi';\mathbf{x},t)d\xi'$$
$$-n(\xi;\mathbf{x},t)\int_0^{\infty}k^A(G;\xi,\xi')n(\xi';\mathbf{x},t)d\xi'$$
$$+\int_{\xi}^{\infty}k^B(G;\xi')b(\xi|\xi')n(\xi';\mathbf{x},t)d\xi'-k^B(G;\xi)n(\xi;\mathbf{x},t) \quad (1)$$

where $n(\xi;\ \mathbf{x},\ t)$ is the Reynolds-averaged CMD; ξ is the dimensionless mass of an aggregate (that is, actual mass divided by mass of primary particles); $\mathbf{x}$ is the spatial coordinate vector, t is physical time; $\langle u_i\rangle$ is the Reynolds-averaged fluid velocity in the ith spatial direction; D_t is the turbulent diffusivity, which in these operating conditions can be approximated by the fluid turbulent diffusivity (see, for example, Baldyga and Orciuch[24]); $k^A(G;\ \xi,\ \xi')$ is the aggregation kernel of two aggregates with masses ξ and ξ', $k^B(G;\ \xi')$ is the breakage kernel of an aggregate of mass ξ'; $b(\xi\,|\,\xi')$ is the daughter distribution function; and G is the shear rate. Equation 1 is derived neglecting fluctuations of the CMD around its mean value on the right-hand side. Moreover, time fluctuations of the shear rate are also neglected and as a first approach only its time-averaged value is considered, as will be explained later. The shear rate in real systems is a spatially dependent property [that is, $G = G(\mathbf{x})$] but for brevity in what follows we will omit this dependency. In turbulent flows the shear rate arising from turbulent fluctuations is defined as[25]

$$G=\sqrt{\frac{\varepsilon}{\nu}} \quad (2)$$

where ε is the turbulent energy dissipation rate and ν is the kinematic viscosity of the suspending fluid. As already reported the turbulent energy dissipation rate, and as a consequence the shear rate, are subjected to time fluctuations around the mean value. This behavior is known as intermittency and can result in instantaneous values of the dissipation rate much higher than the time-averaged one. However, these fluctuations are short lived and are important only for very fast aggregation and the breakage process. In this work these time fluctuations are neglected and only the time-averaged value of the dissipation rate and, consequently, of the shear rate are considered. Nevertheless, as it will become clearer, the effect of spatial variation of the shear rate will be studied. The rigorous model reported in Eq. 1 has to be coupled with continuity Reynolds-averaged Navier–Stokes (RANS) equations and turbulence clo-

sure equations. This results in a computationally intense problem; in fact, the set of equations has to be solved in space and time. In what follows we refer to this approach as the CFD model. The three terms on the left-hand side of Eq. 1 represent time variation, convection, and turbulent diffusion, whereas on the right-hand side the source term quantifies the local rate of variation of the CMD. If the characteristic timescales of these processes (that is, mixing time vs. relaxation time of the CMD) are well separated the two processes can be decoupled. For example, if mixing is much faster than aggregation and breakage then the gradients generated by the right-hand side of Eq. 1 will be immediately destroyed by turbulent mixing. Therefore the CMD will be a function of only time and dimensionless mass and the second and third terms on the left-hand side of Eq. 1 will be null. On the other end if aggregation and breakage are much faster than mixing the CMD in each point of the vessel will relax according to the local value of shear rate. Also in this case the second and third terms on the left-hand side of Eq. 1 will be null because of infinitely small fluid velocity and turbulent diffusion with respect to the source term, although the CMD will still be a function of space.

As already mentioned if mixing is faster than aggregation and breakage, the spatial gradients of the CMD are very small, and thus the CMD can be considered independent with respect to the spatial coordinate and the first two terms on the right-hand side of Eq. 1 can be neglected. We indicate with $\bar{n}(\xi; t)$ the volume-averaged CMD function

$$\bar{n}(\xi; t) = \frac{\int_V n(\xi; \mathbf{x}, t) d\mathbf{x}}{V} \tag{3}$$

where V is the reactor volume and the integral is a three-dimensional integral over the reactor volume. It is clear that under the hypothesis of perfect mixing $\bar{n}(\xi; t) \approx n(\xi; \mathbf{x}, t)$ in each point $\mathbf{x}$ of the reactor. If the volume average is applied to Eq. 1 we obtain

$$\frac{\partial \bar{n}(\xi; t)}{\partial t} = \frac{1}{V} \int_V S(G; \xi) d\mathbf{x} \tag{4}$$

where the source term $S(G; \xi)$ indicates the aggregation and breakage source terms that are contained in the right-hand side of Eq. 1. It is interesting to highlight here that even if mixing is so efficient to smooth down all gradients of the CMD the source term still depends on the spatial coordinate; in fact spatial dependencies are hidden in the shear rate $G = G(\mathbf{x})$. Because spatial dependencies are contained only in the shear rate, we can write that

$$\frac{1}{V} \int_V S(G; \xi) d\mathbf{x} = \int_0^\infty S(G^*; \xi) \frac{\int_V \delta[G^* - G(\mathbf{x})] d\mathbf{x}}{V} dG^* = \int_0^\infty S(G^*; \xi) f(G^*) dG^* = \bar{S}(G; \xi) \tag{5}$$

where $f(G^*)$ is by definition the volume-based distribution of shear rate or, in other words, $f(G^*)dG^*$ represents the volume fraction of the reactor with shear rate in the range between G^* and $G^* + dG^*$. Again by definition

$$1 = \int_0^\infty f(G^*) dG^* \qquad \bar{G} = \int_0^\infty f(G^*) G^* dG^* \tag{6}$$

By explicating the volume average for the aggregation and breakage source terms contained in $S(G; \xi)$ and transporting the volume average inside the integrals over dimensionless mass, we obtain

$$\begin{aligned} \frac{\partial \bar{n}(\xi; t)}{\partial t} = {} & \frac{1}{2} \int_0^\xi \left[\frac{1}{V} \int_V k^A(G; \xi - \xi', \xi') d\mathbf{x} \right] \\ & \times \bar{n}(\xi - \xi'; t) \bar{n}(\xi; t) d\xi' - \bar{n}(\xi; t) \int_0^\infty \left[\frac{1}{V} \int_V k^A(G; \xi, \xi') d\mathbf{x} \right] \\ & \times \bar{n}(\xi'; t) d\xi' + \int_\xi^\infty \left[\frac{1}{V} \int_V k^B(G; \xi') d\mathbf{x} \right] b(\xi|\xi') \bar{n}(\xi'; t) d\xi' \\ & - \left[\frac{1}{V} \int_V k^B(G; \xi) d\mathbf{x} \right] \bar{n}(\xi; t) \end{aligned} \tag{7}$$

where the substitution $n(\xi; \mathbf{x}, t) = \bar{n}(\xi; t)$ is possible because of the hypothesis of perfect mixing and negligible gradients. In a more compact form

$$\begin{aligned} \frac{\partial \bar{n}(\xi; t)}{\partial t} = {} & \frac{1}{2} \int_0^\xi \bar{k}^A(G; \xi - \xi', \xi') \bar{n}(\xi - \xi'; t) \bar{n}(\xi'; t) d\xi' \\ & - \bar{n}(\xi; t) \int_0^\infty \bar{k}^A(G; \xi, \xi') \bar{n}(\xi'; t) d\xi' \\ & + \int_\xi^\infty \bar{k}^B(G; \xi') b(\xi|\xi') \bar{n}(\xi'; t) d\xi' - \bar{k}^B(G; \xi) \bar{n}(\xi; t) \end{aligned} \tag{8}$$

where

$$\bar{k}^A(G; \xi, \xi') = \int_0^\infty k^A(G^*; \xi, \xi') f(G^*) dG^* \tag{9}$$

and

$$\bar{k}^B(G; \xi) = \int_0^\infty k^B(G^*; \xi) f(G^*) dG^* \tag{10}$$

Therefore when mixing is much faster than aggregation and breakage Eq. 8 can be used instead of Eq. 1 and we will refer to this approach as the *homogeneous model*.

In the opposite situation, when aggregation and breakage are much faster than mixing the evolution of the CMD in each point of the computational domain can be tracked independently from the surrounding points. We indicate with $n_\alpha(\xi; t) = n(\xi; \mathbf{x}_\alpha, t)$ the CMD in a specific location $\mathbf{x}_\alpha$ with corresponding shear rate $G_\alpha = G(\mathbf{x}_\alpha)$. The evolution equation for the CMD function in each point of the computational domain is

$$\frac{\partial n_\alpha(\xi; t)}{\partial t} = \frac{1}{2}\int_0^\xi k^A[G(\mathbf{x}_\alpha); \xi - \xi', \xi']n_\alpha(\xi - \xi'; t)n_\alpha(\xi'; t)d\xi' - n_\alpha(\xi; t)\int_0^\infty k^A[G(\mathbf{x}_\alpha); \xi, \xi']n_\alpha(\xi'; t)d\xi' + \int_\xi^\infty k^B[G(\mathbf{x}_\alpha); \xi']b(\xi|\xi')n_\alpha(\xi'; t)d\xi' - k^B[G(\mathbf{x}_\alpha); \xi]n_\alpha(\xi; t) \quad (11)$$

It is clear that, if the initial condition is the same for all points of the physical domain (that is, primary particles), different points with the same local shear rate G_α will result in the same evolution of the CMD. Therefore the volume-averaged CMD function can be calculated as usual

$$\bar{n}(\xi; t) = \frac{1}{V}\int_V n(\xi; \mathbf{x}_\alpha, t)d\mathbf{x}_\alpha = \int_0^\infty n(\xi; G_\alpha, t)f(G_\alpha)dG_\alpha \quad (12)$$

In what follows we will refer to this as to the *instantaneous equilibrium model*. As mentioned earlier the instantaneous equilibrium model is based on the idea that the CMD relaxes much faster than spatial gradients of the CMD at the macroscale level. Therefore the limit of this approach is based in the fact that when the CMD also relaxes faster than the characteristic time for turbulent fluctuations then a micromixing model is needed. Accordingly, in the following we consider the case where the characteristic time of micromixing is very small compared to that of macromixing (that is, at the vessel scale) and of the aggregation and breakage processes.

In many situations the distribution of shear rate is not known and only its mean value $\bar{G}$ can be estimated. If the distribution is assumed to be a delta Dirac function centered on its mean value (that is, all regions of the reactor operate at the same value of shear rate equal to the mean value) we obtain

$$\frac{\partial \bar{n}(\xi; t)}{\partial t} = \frac{1}{2}\int_0^\xi k^A(\bar{G}; \xi - \xi', \xi')\bar{n}(\xi - \xi'; t)\bar{n}(\xi'; t)d\xi' - \bar{n}(\xi; t)\int_0^\infty k^A(\bar{G}; \xi, \xi')\bar{n}(\xi'; t)d\xi' + \int_\xi^\infty k^B(\bar{G}; \xi')b(\xi|\xi')\bar{n}(\xi'; t)d\xi' - k^B(\bar{G}; \xi)\bar{n}(\xi; t) \quad (13)$$

and we will refer to this as the *lumped model*. Note that this model coincides with the homogeneous model Eq. 8 defined above, except in the evaluation of the rate constants k^A and k^B. If the hydrodynamic in the vessel is uniform—that is, the shear distribution is a Dirac delta—then the two models coincide; if not, the lumped model may lead to significant overpredictions.

Aggregation and Breakage Kernels

We now need to define the functional form of the aggregation and breakage kernels. We consider the aggregation kernel for destabilized colloidal particles defined as the summation of two contributions, one arising from Brownian motions and the second from fluid shear[26]

$$k^A(G; \xi, \xi') = \frac{2k_BT}{3\mu}\frac{1}{W}(\xi^{1/d_f} + \xi'^{1/d_f})(\xi^{-1/d_f} + \xi'^{-1/d_f}) + \alpha_A(\xi, \xi')GR_p^3(\xi^{1/d_f} + \xi'^{1/d_f})^3 \quad (14)$$

where k_B is the Boltzman constant, T is the absolute temperature, μ is the fluid viscosity, W is the stability ratio, d_f is the fractal dimension of aggregates, $\alpha_A(\xi, \xi')$ is the aggregation prefactor, and R_p is the radius of primary particles. This formulation is based on the description of aggregates as fractal-like objects, where their radius scales with mass as[27-29]

$$R = R_p\xi^{1/d_f} \quad (15)$$

Here we assume for simplicity that collision, hydrodynamic, and gyration radii are equal, although they differ slightly up to a multiplicative constant close to unity, as has been shown through Monte Carlo simulations[30,31] and experimental observations.[32] This scaling relation has been used in Eq. 14 to replace all terms containing hydrodynamic and collision radii by their dimensionless masses using fractal scaling in Eq. 15. It is known that the two parameters of the aggregation kernel, W and $\alpha_A(\xi, \xi')$, are complex functions of size of primary particles, physicochemical properties of the material constituting the primary particles, and liquid-phase composition.[33] Moreover, fractal scaling prefactors can be folded into these parameters. Therefore, in general, they have to be estimated by fitting an appropriate set of experimental data. Because the main objective of this work is to illustrate the effect of spatial heterogeneity of the shear rate on the CMD, here we use typical parameter values taken from the literature as discussed later.

With respect to breakage, two different approaches can be used. Breakage is caused by shear rate, which produces hydrodynamic stresses that can break the aggregate when they overcome cohesive forces holding particles together. The breakage rate of an aggregate of dimensionless mass ξ with radius R (see Eq. 15) can be expressed as follows[3]

$$k^B(G;\,\xi) = \left(\frac{4}{15\pi}\right)^{1/2} G\,\exp\left[\frac{-B(G)}{G^2 R_p \xi^{1/d_f}}\right] \tag{16}$$

This expression is known as the exponential breakage kernel, where B is usually expressed as a power-law function of shear. An alternative description of the breakage rate is the so-called power-law kernel

$$k^B(G;\,\xi) = P_1 G^{P_2} (R_p \xi^{1/d_f})^{P_3} \tag{17}$$

where P_1, P_2, and P_3 are adjustable parameters. Another important component of the model is the daughter distribution function $b(\xi\,|\,\xi')$, which contains information about the size of the fragments ξ produced by breaking up an aggregate of mass ξ'. For example, if a breakage event produces n fragments with equal masses ξ'/n, the daughter distribution function is as follows

$$b(\xi|\xi') = \sum_{i=1}^{n} \delta\left(\xi - \frac{\xi'}{n}\right) \tag{18}$$

In the case of formation of two fragments with mass ratio equal to a, the daughter distribution function becomes

$$b(\xi|\xi') = \delta\left(\xi - \frac{1}{1+a}\,\xi'\right) + \delta\left(\xi - \frac{a}{1+a}\,\xi'\right) \tag{19}$$

Solution of the Population Balance Equations

There are several approaches available in the literature for the solution of Eq. 1, such as method of successive approximations, method of Laplace transforms, method of moments, method of weighted residual, classes method, and Monte Carlo simulations.[23] Here we discuss only two of these approaches: the method of moments (MOM) and the classes method (CM).

Method of moments

The MOM simply consists of solving transport equations for the moments of the CMD instead of the original PBE.[34] The moment of order k of the CMD is defined as

$$m_k(\mathbf{x},\,t) = \int_0^\infty n(\xi;\,\mathbf{x},\,t)\xi^k d\xi \tag{20}$$

and it is clear that m_0 represents the total particle number density and m_1 is the total mass. By applying the moment transform to the PBE it is possible to obtain the transport equation for each moment m_k

$$\frac{\partial m_k(\mathbf{x},\,t)}{\partial t} + \frac{\partial}{\partial x_i}\left[\langle u_{ik}\rangle m_k(\mathbf{x},\,t)\right] - \frac{\partial}{\partial x_i}\left[D_t \frac{\partial m_k(\mathbf{x},\,t)}{\partial x_i}\right] = \frac{1}{2}\int_0^\infty \int_0^\infty [(\xi+\xi')^k - \xi^k - \xi'^k] k^A(G;\,\xi,\,\xi') n(\xi;\,\mathbf{x},\,t) n(\xi';\,\mathbf{x},\,t) d\xi' d\xi + \int_0^\infty \xi^k \int_0^\infty k^B(G;\,\xi') b(\xi|\xi') n(\xi';\,\mathbf{x},\,t) d\xi' d\xi - \int_0^\infty k^B(G;\,\xi) n(\xi;\,\mathbf{x},\,t)\xi^k d\xi \tag{21}$$

with $k \in 0,\,1,\,2,\,3,\cdots$ and where $\langle u_{ik}\rangle$ is the velocity with which each moment is transported. It is easy to show that

$$\langle u_{ik}\rangle = \frac{\int_0^\infty \langle u_i\rangle n(\xi;\,\mathbf{x},\,t)\xi^k d\xi}{m_k(\mathbf{x},\,t)} \tag{22}$$

and it is also clear that if $\langle u_i\rangle$ is not a function of ξ then all moments are transported with the same velocity (that is, $\langle u_{ik}\rangle = \langle u_i\rangle$ with $k \in 0,\,1,\,2,\,3,\cdots$). This is the case of the investigated process.

The main problem related to this approach stands in the fact that it is very difficult to express Eq. 21 in terms of moments of order equal to or less than k and this is known as the "closure problem." [34] Several techniques have been developed[35] and one of the most accurate and promising is indeed the quadrature method of moments (QMOM).[36] This technique has been applied in length-based formulation and validated for aggregation breakage problems,[37,38] implemented in a CFD code,[18] formulated in a direct way,[39-41] and applied for the solution of bivariate problems.[42-44] Moreover, the QMOM has been also applied in a volume-based form but in operating conditions very different from those of this work.[45]

The closure problem in QMOM is overcome by using a quadrature approximation. The quadrature approximation is built determining the sequence of polynomials orthogonal to the "measure" $n(\xi)$ (that is, the CMD). If the abscissas of the quadrature approximation are the nodes of the polynomial of order N, the following quadrature approximation

$$\int_0^\infty n(\xi)\,f(\xi)\,d\xi \approx \sum_{i=1}^{N} f(\xi_i) w_i \tag{23}$$

is exact if $f(\xi)$ is a polynomial of order N or smaller.[46] In all the other cases the approximation is the more accurate the closer $f(\xi)$ is to a polynomial. A direct way to calculate the quadrature approximation is by means of its definition through the moments

$$m_k = \sum_{i=1}^{N} w_i \xi_i^k \tag{24}$$

In fact, the quadrature approximation of order N is defined by its N weights w_i and N abscissas L_i and can be calculated by its first $2N$ moments $m_0, \ldots, m_{2N-1}$. This nonlinear system can be solved by using the Newton–Rapson method or any other nonlinear equations solver, although this is not the best way because a very good initial guess is needed. A smarter way is to write the recursive relationship for the polynomials in terms of the moments m_k. Once this relationship is written in matrix form it is easy to show that the roots of the polynomials

correspond to the eigenvalues of the so-called Jacobi matrix (see algorithm *gaucof* reported by Press[47]). This is the procedure used in the *product–difference* (PD) algorithm, which was found to be stable in all the tested cases.[48]

Once weights and abscissas are known, the source terms attributed to coalescence and breakage can be calculated and therefore the transport equations for the moments can be solved. A detailed description of the algorithm and its mathematical derivation is reported in the Appendix. The transport equation for the moment m_k, applying the quadrature approximation, results in

$$\frac{\partial m_k(\mathbf{x}, t)}{\partial t} + \frac{\partial}{\partial x_i}[\langle u_i \rangle m_k(\mathbf{x}, t)] - \frac{\partial}{\partial x_i}\left[D_t \frac{\partial m_k(\mathbf{x}, t)}{\partial x_i}\right] = \frac{1}{2}\sum_{i=1}^{N}\sum_{i=1}^{N}[(\xi_i + \xi_j)^k - \xi_i^k - \xi_j^k]k_{i,j}^A w_i w_j + \sum_{i=1}^{N} k_i^B \bar{b}_i^{(k)} w_i - \sum_{i=1}^{N} \xi_i^k k_i^B w_i \quad (25)$$

where $k_{ij}^A = k^A(G; \xi_i, \xi_j)$ and $k_i^B = k^B(G; \xi_i)$ and the moment of the daughter distribution function is

$$\bar{b}_i^{(k)} = \int_0^\infty \xi^k b(\xi|\xi_i) d\xi \quad (26)$$

It is useful to point out here that the abscissas and weights appearing in Eq. 25 are functions of space and time [that is, $\xi_i = \xi_i(\mathbf{x}, t)$ and $w_i = w_i(\mathbf{x}, t)$] because they are calculated by the local values of the moments of the CMD by using the PD algorithm.

Classes methods

There are several classes methods and a comparison of performances in terms of accuracy, computational time, and ease of implementation can be found in the work by Vanni.[49] The classes method is based on the idea of discretizing the internal coordinate into a number of finite bins (that is, $\xi_1, \xi_2, \ldots, \xi_M$), and therefore the representation of the CMD function is

$$n(\xi; \mathbf{x}, t) = \sum_{i=1}^{M} N_i(\mathbf{x}, t)\delta(\xi - \xi_i) \quad (27)$$

If a linear discretization is used (that is, $\xi_1 = 1, \xi_2 = 2, \ldots, \xi_i = i$), then the PBE is rigorously solved and the transport equation for each cluster class is

$$\frac{\partial N_i(\mathbf{x}, t)}{\partial t} + \frac{\partial}{\partial x_i}[\langle u_i \rangle N_i(\mathbf{x}, t)] - \frac{\partial}{\partial x_i}\left[D_t \frac{\partial N_i(\mathbf{x}, t)}{\partial x_i}\right] = \frac{1}{2}\sum_{j=1}^{i-1} k_{i-j,j}^A N_{i-j}(\mathbf{x}, t) N_j(\mathbf{x}, t) - N_i(\mathbf{x}, t)\sum_{j=1}^{\infty} k_{i,j}^A N_j(\mathbf{x}, t) + \sum_{i=1+1}^{\infty} k_j^B b_{ij} N_j(\mathbf{x}, t) - k_i^B N_i(\mathbf{x}, t) \quad (28)$$

where $k_{ij}^A = k^A(G; \xi_i, \xi_j)$, $k_i^B = k^B(G; \xi_i)$, and $b_{ij} = b(\xi_i \mid \xi_j)$ and where the summations are extended up to infinity to cover the entire size range. Because the classes to be tracked in a real application would be too many it is necessary to resort to approximate models. The approach by Batterham[50] is based on a geometric grid with constant mass ratio equal to 2.0 (that is, $\xi_{i+1} = 2\xi_i$). Hounslow[51] used this discretization scheme and identified four types of processes that result in a set of consistent equations conserving the total particle number density (m_0) and the total particle mass (m_1). More recently, Kumar and Ramkrishna[52] proposed a discretization technique that allows the conservation of two moments of the distribution. Details about these two population balance models can be found in the original papers.

Case Studies and Numerical Details

Aggregation and breakage are investigated in this work in the Taylor–Couette reactor. This vessel is composed of two concentric cylinders, the inner one of which rotates and the outer is at rest. The fluid is contained in the gap between the two cylinders and, depending on the rotational speed of the inner cylinder, several fluid dynamic regimes can be achieved. A complete review on the fluid dynamic regimes in this kind of reactor is reported in the work by Kataoka.[53] The diameter of the inner cylinder is 124 mm, whereas the diameter of the outer cylinder is 140 mm, resulting in an annular gap of 8 mm. The reactor height is 320 mm. The rotational speed of the inner cylinder is kept within the range of 50 and 100 rpm because in this range the flow is in the so-called turbulent Taylor vortex flow region and the range of shear rate is between 75 and 150 s^{-1}.

The reactor is modeled with the commercial CFD code FLUENT (Fluent, Inc., Lebanon, NH) under the hypothesis of axial symmetry, resulting in a two-dimensional axial-symmetric grid. Previous validations of the CFD predictions by using laser Doppler anenometry (LDA)[54] showed that the Reynolds stress model coupled with standard wall functions gives the best agreement for the predicted Reynolds-averaged velocities and Reynolds stresses. The entire meridian section of the reactor has been modeled with FLUENT and a grid-independent solution was found for 21 nodes in the radial direction and 321 in the axial direction. Moreover, two reduced geometries have been investigated: in the first one only a part of the meridian section corresponding to a length twice the annular gap has been considered, whereas in the second one a length corresponding to four times the annular gap has been considered. In both cases symmetry boundary conditions were used for the upper and lower sections. Comparison between the predictions of the full cell and one section corresponding to a couple of vortices (that is, length equal to twice the annular gap) and one section corresponding to two couples of vortices (that is, length equal to four times the annular gap) showed very similar results in terms of Reynolds-averaged velocities. However, to correctly describe the shear rate distribution in the vessel the section containing two couples of vortices was used for the simulation of the aggregation and breakage process.

With respect to aggregation and breakage simulations, the CFD model was solved by using user-defined subroutines in FLUENT. Because of the intractable number of scalars required by the fixed-pivot method and the sectional method (that

is, about 80 in the first case and 20 in the second, as will be made clearer later) the CFD model has been implemented using only QMOM. Transport equations for the moments were defined through their source terms by means of define-source subroutines, whereas the PD algorithm and aggregation and breakage kernels were defined in the define-adjust subroutine. The PD algorithm was implemented by using the subroutine *imtql2* of the package for linear algebra EISPACK.[47] The moments were transported in physical space with the same velocity equal to the fluid velocity calculated by considering only the liquid phase. According to Baldyga and Orciuch,[24] in fact, solid particles can be assumed to follow the fluid streamlines and the influence of the solid phase on flow and turbulence fields of the liquid phase can be neglected for solid concentrations < 0.1–1.0%, which in terms of the solids volume fraction corresponds to $\phi_s = 1.0 \times 10^{-3}$ to 1.0×10^{-2}.

The time-dependent calculations were performed with a fixed time step. Convergence at each time step was achieved when all the residuals of the user-defined scalars were $<1.0 \times 10^{-6}$. Great care must be taken in the choice of the time step because it substantially affects the accuracy of the calculations. At low concentration a time step of about 10 s can be used, but for higher concentrations the time step has to be reduced to 1.0×10^{-3}. Calculations for the lumped model were performed with the QMOM, the fixed-pivot, and the sectional methods to compare the performances of the three population-balance models in terms of accuracy and computational time. All calculations outside the CFD code FLUENT were performed using the ODE solver *lsode* based on the backward differentiation formula, a modification of the Adams method for stiff problems of the ODE solver package ODEPACK. For both homogeneous and instantaneous equilibrium models it is required to provide the volume shear rate distribution $f(G)$ that can be easily extracted from the FLUENT data file.

In this work we used the same primary particles diameter ($2.17\ \mu$m) and range of shear rate (75–150^{-1}) as in the experimental work of Oles.[5] The parameters in the aggregation and breakage kernel have been determined by fitting the experimental data reported in the same work. Because this reports only the average value of the shear rate, this fitting procedure was performed using the lumped model and the parameters were estimated in the range of shear rates $75 < G < 150\ \text{s}^{-1}$. The estimated values of the aggregation kernel parameters in Eq. 14 are $d_f = 2.1$, $\alpha_A(\xi, \xi') = 0.15$, $W = 1.0$, whereas for breakage kernel parameters we obtained for the exponential breakage kernel (Eq. 16): $B = 9.0 \times 10^{-10} G^{1.5}$ and for the power-law breakage kernel (Eq. 17): $P_1 = 1.55 \times 10^{12}$, $P_2 = 2.82$, and $P_3 = 4$. In both cases binary symmetric breakage was used and therefore the daughter distribution function is given by

$$b(\xi|\xi') = 2\delta\left(\xi - \frac{\xi'}{2}\right) \tag{29}$$

and after moment transformation

$$\bar{b}_i^{(k)} = 2^{1-k}\xi_i^k \tag{30}$$

It is important to note that because the aim of the work is to numerically investigate the effect of spatial heterogeneities, the kinetic parameters have to represent a realistic system, although a fine-tuning on a specific system would not be appropriate.

Small-Angle Light Scattering

To characterize populations of aggregates of colloidal primary particles we need to choose quantities that can be experimentally measured and at the same time calculated from the cluster mass distribution obtained from a population balance model. For this we need a reliable model of aggregate properties relevant for the particular measurement.[55,56] Here we consider static light scattering (SLS) because sound models for optical properties of fine particles and fractal aggregates are available, allowing us to calculate the same quantities as those obtained from SLS measurements, that is, the mean radius of gyration $\langle R_g \rangle$ and the mass-weighted mean mass, proportional to the zero-angle intensity $I(0)$. These quantities are in fact moments of the underlying cluster mass distribution of the population of aggregates and describe certain well-defined average properties of this population. In particular, the mean radius of gyration is given by

$$\langle R_g^2 \rangle = \frac{\sum_{i=1}^{N} N_i i^2 R_{g,i}^2}{\sum_{i=1}^{N} N_i i^2} \tag{31}$$

where $R_{g,i}$ is the radius of gyration of an aggregate constituted by i primary particles, as defined in Eq. 15, and where N_i is the number density of aggregates of dimensionless size $i = \xi_i$. The zero-angle intensity is instead given by

$$I(0) = \frac{\sum_{i=1}^{N} N_i i^2}{\sum_{i=1}^{N} N_i i} \tag{32}$$

The principle of SLS is based on the measurement of the intensity of scattered light I as a function of the scattering wave vector q. The scattering vector amplitude is a function of scattering angle θ, refractive index of the dispersant n, and wavelength in vacuo of laser light λ

$$q = 4\pi \frac{n}{\lambda} \sin\frac{\theta}{2} \tag{33}$$

The scattered light intensity $I(q)$ can be factored into a product of the zero-angle intensity $I(0)$, the form factor of primary particles $P(q)$, and the averaged structure factor of aggregates $S(q)$.[1] If primary particles are small enough, then one can simply use the intensity $I(q)$ instead of the structure factor $S(q)$, given that $P(q)$ is close to unity. In any case, the form factor $P(q)$ can be either computed from the Mie theory for spherical particles or measured using the initial dispersion of primary particles.

It is worth noting some characteristic regions of $I(q)$ from SLS measurement. At small q values ($q \ll 1/R_g$) the intensity reaches a limiting value equal to $I(0)$. In the Gunier region ($q < 1/R_g$) it is possible to determine both the zero-angle intensity $I(0)$ and the mean radius of gyration $\langle R_g \rangle = \langle R_g^2 \rangle^{1/2}$ from the Zimm plot,[57] routinely used to characterize dilute polymer solutions. If the aggregates are fractal objects, then the struc-

ture factor exhibits a power-law behavior in the region ($1/R_g < q < 1/R_p$). The slope of $\log[S(q)]$ as a function of $\log(q)$, in the case where primary particles are small enough and all aggregates contain a sufficiently large number of primary particles, represents the fractal dimension of the aggregates. As was discussed earlier, in the population-balance model implemented here we use fractal scaling between aggregate size and mass for all aggregates. Strictly speaking, such scaling relationship is accurate only for sufficiently large aggregates.[31] In our case, this condition is not satisfied in the very early stage of the aggregate growth. For very small clusters, we should use specific expressions for their radius of gyration, such as $R_g(1) = \sqrt{3/5}R_p$ and $R_g(2) = \sqrt{8/5}R_p$. On the other hand, the error made assuming fractal scaling even for trimers is $<10\%$, and rapidly decreases as the aggregates mass increases.[31] Considering that at the steady-state conditions examined in this work most of the aggregates are quite large, Eq. 31 has been used for all aggregate sizes.

Results and Discussion

As a first step the QMOM, the fixed-pivot, and the sectional methods are compared in the frame of the lumped model discussed above, using the kinetic parameters reported above for both the exponential and the power-law breakage kernel.

Comparison of numerical methods for the solution of population-balance models

This part of the work aims to analyze the performance of the three approaches in solving the population-balance equation independently to the description of spatial heterogeneity. Results are reported in terms of two integral properties of the CMD: the mean radius of gyration relative to the radius of primary particles and the relative zero-angle intensity. These two quantities are given by Eqs. 31 and 32, and can be expressed in terms of the quadrature approximation using fractal scaling (see Eq. 15) as follows

$$\frac{\langle R_g \rangle}{R_p} = \sqrt{\frac{\sum_{i=1}^{N} w_i \xi_i^{2(1+1/d_f)}}{\sum_{i=1}^{N} w_i \xi_i^2}} \tag{34}$$

$$I(0) = \frac{\sum_{i=1}^{N} w_i \xi_i^2}{\sum_{i=1}^{N} w_i \xi_i} \tag{35}$$

By replacing the weights of the quadrature approximation w_i with population class densities N_i, Eqs. 34 and 35 can be used for the class method (CM).

Note that for primary particles and very small clusters Eq. 34 is an approximation, which for populations primarily composed of larger aggregates does not lead to significant errors. The QMOM with a quadrature approximation with $N = 2, 3, 4$, and 5 has been compared with the sectional method based on a geometric discretization with aggregate mass ratio equal to 2.0, and with the fixed-pivot method with a linear discretization for the first 16 classes and with a geometric discretization with mass ratio equal to $17/16 = 1.0625$ for the remaining ones. It is interesting to note that for this particular application, to cover the range of interest of dimensionless mass, the fixed-pivot method requires the use of 80 classes, whereas the sectional method requires the use of 20 classes. QMOM, however, which is based on the solution of transport equations for the moments, contains information for an arbitrary range of aggregate mass. Solution of QMOM with two nodes ($N = 2$) requires tracking of the first four moments of the CMD, QMOM with three nodes ($N = 3$) requires six moments, QMOM $N = 4$ requires eight moments, and QMOM $N = 5$ requires ten moments. It is clear that use of QMOM reduces the number of scalars to be tracked, which is a crucial advantage in CFD simulation, where for each additional scalar a transport equation needs to be solved. Clearly this is achieved at the expense of accuracy, although detailed comparison with alternative methods[36-38,45] indicates a satisfactory behavior. However, the method has never been tested in the volume-based formulation and for the low values of fractal dimension considered in this work.

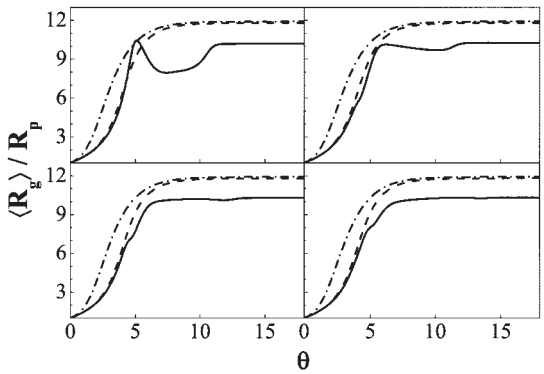

Figure 1. Comparison of $\langle R_g \rangle / R_p$ between QMOM (solid line), fixed-pivot (dash line), and sectional (dash–dot line) methods for exponential breakage kernel.

$\bar{G} = 110\ s^{-1}$; $\phi_s = 5.0 \times 10^{-5}$. From top to bottom and left to right QMOM $N = 2$, 3, 4, and 5.

Figure 1 compares the radius of gyration, as a function of dimensionless time $\theta = tG\phi_s$, predicted by the various methods under examination for volume-averaged shear rate $G = 110\ s^{-1}$ and solids volume fraction $\phi_s = 5.0 \times 10^{-5}$. The results plotted in this figure refer to the aggregation kernel reported in Eq. 14 and the exponential breakage kernel reported in Eq. 16 by using the parameters determined by fitting the experimental data of Oles.[5] By taking the fixed-pivot method as a reference, which is the most accurate, it is seen that QMOM, notwithstanding the number of nodes used in the quadrature approximation, is able to track very accurately the early CMD evolution, whereas the sectional method always overpredicts the mean radius of gyration. To improve the QMOM description of the late dynamics, a number of nodes greater than four must be used and therefore more than eight moments of the CMD must be tracked. It is interesting to point out that little improvement in the prediction of the steady state is achieved by increasing the number of nodes of the quadrature approximation. The corresponding comparison for the relative zero-angle intensity is shown in Figure 2. It is found that the comparison is qualitatively similar but the general agreement is worse. This result is surprising because the relative zero-angle intensity is equal to m_2/m_1, involving lower-order moments than the radius of gyration, which is proportional to $\sqrt{m_3/m_2}$ (if $d_f = 2$), and usually the prediction for lower-order moments is better than

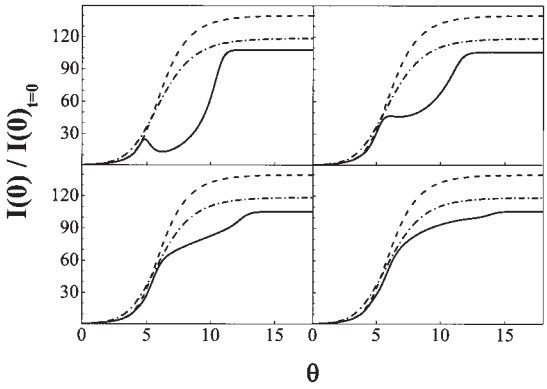

Figure 2. Comparison of $I(0)/I(0)_{t=0}$ between QMOM (solid line), fixed-pivot (dash line), and sectional (dash–dot line) methods for exponential breakage kernel.

$\bar{G} = 110\ s^{-1}$; $\phi_s = 5.0 \times 10^{-5}$. From top to bottom and left to right QMOM $N = 2$, 3, 4, and 5.

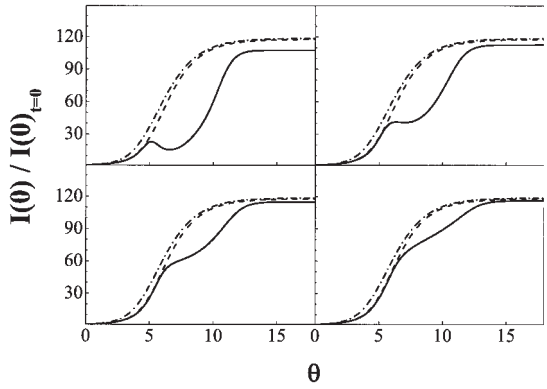

Figure 4. Comparison of $I(0)/I(0)_{t=0}$ between QMOM (solid line), fixed-pivot (dash line), and sectional (dash–dot line) methods for power-law breakage kernel.

$\bar{G} = 110\ s^{-1}$; $\phi_s = 5.0 \times 10^{-5}$. From top to bottom and left to right QMOM $N = 2$, 3, 4, and 5.

that for higher-order moments. This can be understood by considering that, because QMOM correctly computes the total mass m_1, the error in m_2 appears directly in the relative zero-angle intensity, whereas some compensation between the errors in m_2 and m_3 is possible when calculating the radius of gyration.

In Figures 3 and 4 the same comparison as above is reported for the power-law kernel (see Eq. 17). It is seen that in this case the performance of QMOM is significantly improved in terms of both the radius of gyration and the zero-angle intensity. This is attributed to the power-law form of the breakage kernel (see Eq. 17), which can be better described by polynomials of order N. In particular, the radius of gyration predicted by QMOM is very close to that predicted by the fixed-pivot method, whereas the sectional method overpredicts the early dynamics as well as the steady-state value. For the relative zero-angle intensity the situation is very similar, although the QMOM prediction of the dynamic behavior is somewhat worse. The sectional method overpredicts the early dynamics but then gets closer to the fixed-pivot method at longer times. It is interesting to note that for this breakage kernel the three methods compute the same steady-state value of the relative zero-angle intensity.

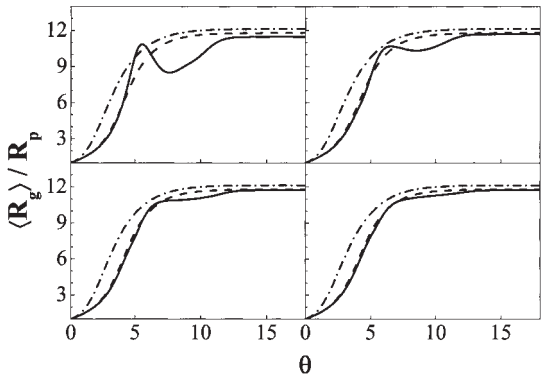

Figure 3. Comparison of $\langle R_g \rangle / R_p$ between QMOM (solid line), fixed-pivot (dash line), and sectional (dash–dot line) methods for power-law breakage kernel.

$\bar{G} = 110\ s^{-1}$; $\phi_s = 5.0 \times 10^{-5}$. From top to bottom and left to right QMOM $N = 2$, 3, 4, and 5.

It merits mentioning that, with respect to previous analyses,[18,37,38] the performance of QMOM evidenced in Figures 1 and 3 is not as satisfactory. This is related to two aspects. First, in the previous applications the highest moment tracked with the quadrature approximation was M_9 in the length-based formulation, corresponding to m_3 in the volume-based distribution, but the highest moment actually used for comparison and validation was M_4, corresponding to $m_{4/3}$ in the volume-based formulation, which is a moment of much lower order than those considered in this work. It is thus clear that the problem is not in the choice of the set of moments tracked, but in the highest order of the moment considered in the comparison. Tests with different sets of moments (using, say, fractional order moments) are reported in another work[58] and we refer to this work for details. Second, in the specific application considered here the fractal dimension is rather small, which leads to a very steep exponential breakage kernel (see Eq. 16). Like the quadrature approximation itself, the QMOM method can do little in this case, particularly when we impose a very small number of quadrature points.

From the preceding results it is seen that, although the disagreement is reduced when the number of nodes is increased, with both kernels there is a common problem for the intermediate dynamic behavior and more precisely when θ is between 5 and 10. This can be explained by comparing the position of the nodes in the particle mass phase space with the CMD calculated with the fixed-pivot method as shown in Figures 5 and 6 at time $\theta = 7.5$ and 15, respectively. For the early stages of aggregation the agreement is very good, but when breakage starts to play a bigger role, additional small clusters are produced and repopulate the lower classes of the CMD that were depleted because of aggregation. In Figure 5 it is seen that the lower tail of the CMD is equally important with respect to the upper tail. If only two nodes are available the polydispersity cannot be accurately represented by QMOM. In the case of a larger number of nodes, one node is always in the lower tail, representing the small clusters produced by break-

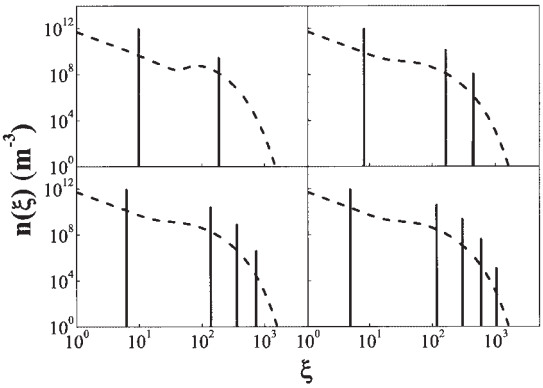

Figure 5. Comparison of CMD predicted by the QMOM (vertical bars) and the fixed-pivot (dash line) methods for power-law breakage kernel.

$\bar{G} = 110\ s^{-1}$; $\phi_s = 5.0 \times 10^{-5}$; dimensionless time $\theta = 7.5$. From top to bottom and left to right QMOM $N = 2$, 3, 4, and 5.

age, whereas the others are used by the PD algorithm to represent the bulk of big aggregates. As soon as aggregation and breakage equilibrate, the tail at lower sizes becomes much less important so that the algorithm can concentrate all the nodes in the portion of larger sizes (see Figure 6), thus leading to better accuracies.

Comparison of the models in different operating conditions (that is, higher shear rates and higher solids volume fractions) confirmed the results discussed above. Therefore we can conclude that QMOM is a useful approach for treating these problems because it is able to predict integral properties of the CMD with acceptable accuracy with a small number of scalars. In particular, if no steep functions, such as the exponential breakage kernel, are involved in the model and if one is interested in computing the steady-state CMD, QMOM with two nodes (that is, tracking the first four moments) is sufficient. This requires the solution of four transport equations vs. 20 for the sectional and 80 for the fixed-pivot method, and is therefore suitable to be used in a CFD code. If the dynamic behavior has

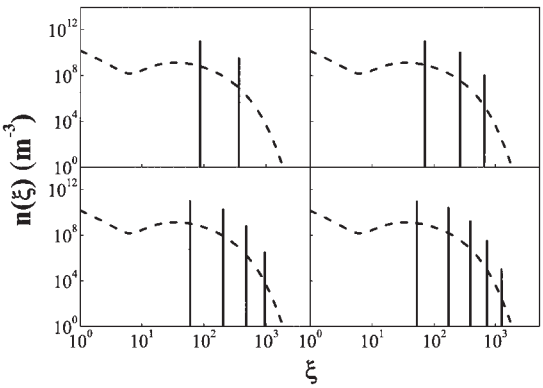

Figure 6. Comparison of CMD predicted by the QMOM (vertical bars) and the fixed-pivot (dash line) methods for power-law breakage kernel.

$\bar{G} = 110\ s^{-1}$; $\phi_s = 5.0 \times 10^{-5}$; dimensionless time $\theta = 15$. From top to bottom and left to right QMOM $N = 2$, 3, 4, and 5.

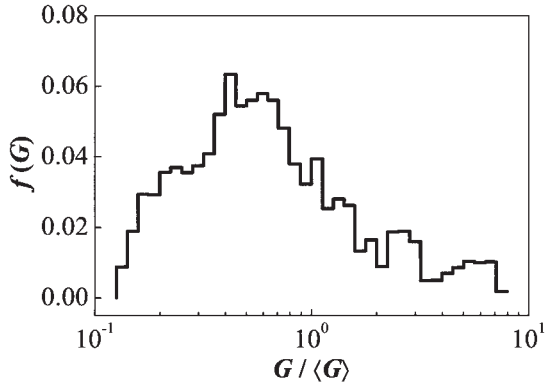

Figure 7. Shear rate distributions in Taylor–Couette reactor for $\bar{G} = 110\ s^{-1}$ calculated with CFD.

to be simulated, then QMOM with four nodes is an acceptable trade-off between computational cost and accuracy. Also in this case the advantage of using QMOM is evident: eight scalars vs. 20 and 80 for the other two methods.

Taylor–Couette reactor

The CFD (solved with QMOM with $N = 4$), homogeneous, instantaneous equilibrium, and lumped models are now compared using the kinetic parameters reported in the previous section with the power-law breakage kernel. The shear rate distribution in the Taylor–Couette reactor is reported in terms of the normalized shear rate in Figure 7. If the volume-averaged kinetic parameters appearing in Eq. 8 are expressed using Eqs. 14 and 17 we obtain

$$\bar{k}^A(G;\,\xi,\,\xi') = \int_0^\infty k^A(G;\,\xi,\,\xi')\,f(G^*)\,dG^* = \frac{2k_BT}{3\mu}\,\frac{1}{W}\,(\xi^{1/d_f} + \xi'^{\,1/d_f})(\xi^{-1/d_f} + \xi'^{\,-1/d_f}) + \alpha_A(\xi,\,\xi')\bar{G}R_p^3(\xi^{1/d_f} + \xi'^{\,1/d_f})^3 \quad (36)$$

and

$$\bar{k}^B(G;\,\xi) = \int_0^\infty k^B(G;\,\xi)\,f(G^*)\,dG^* = P_1\overline{G^{P_2}}(R_p\xi^{1/d_f})^{P_3} \quad (37)$$

These equations show that with respect to aggregation there is no difference in using the homogeneous model or the lumped model, that is, $\bar{k}^A = k^A(\bar{G})$, because the aggregation kernel depends linearly on shear rate, although there is an obvious difference in terms of the breakage kernel, given that $\overline{G^{P_2}} \neq \bar{G}^{P_2}$.

In Figure 8 the comparison of the evolution of the radius of gyration vs. dimensionless time θ for solids volume fraction $\phi_s = 5.0 \times 10^{-5}$ predicted by the different models (that is, CFD, lumped, and homogeneous) is shown. It is seen that the agreement between the homogeneous and the CFD model is excellent, whereas the lumped model overpredicts the radius of gyration. This is caused by the fact that the lumped model ignores the shear rate distribution, approximating it with a Dirac delta function centered on the mean value, resulting in a

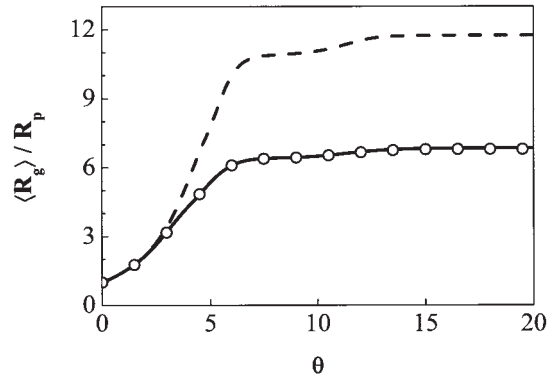

Figure 8. $\langle R_g \rangle / R_p$ as a function of dimensionless time predicted by the CFD (solid line), lumped (dash line), and homogeneous (open circles) models.

$\bar{G} = 110\ s^{-1}$; $\phi_s = 5.0 \times 10^{-5}$; Taylor–Couette reactor.

strong underestimation of the breakage rate. It is worth comparing the predictions of the models for various shapes of the shear rate distribution while keeping its mean value constant. For this we replace (in each cell of the computational domain) the value of G by G' defined as

$$G' = \bar{G}(1 - b) + Gb \tag{38}$$

Thus, by changing b we obtain a family of distributions with different shapes but the same mean value. By inspection of the results shown in Figure 8, which correspond to the distribution with $b = 1$, and those shown in Figure 9 corresponding to b values of 0.25, 0.5, and 0.75, we conclude that the narrower the distribution (that is, b values decrease from 1.0 to 0.0), the more accurate the value of the lumped model, which becomes exact at $b = 0$. Also in this case the comparison between the homogeneous model and the CFD model shows excellent

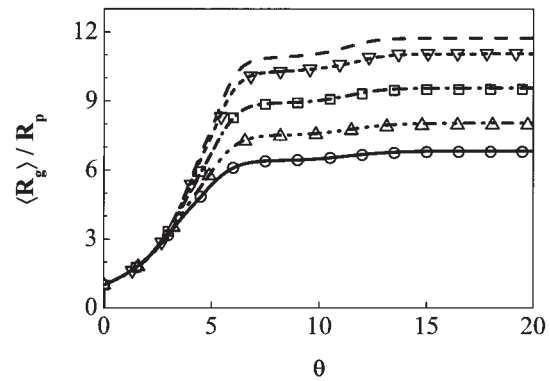

Figure 9. $\langle R_g \rangle / R_p$ as a function of dimensionless time predicted by various models for the different shear rate distributions with the same average value $\bar{G} = 110\ s^{-1}$ for $\phi_s = 5.0 \times 10^{-5}$.

Lumped model (dash line) for $b = 0.0$; CFD model (open inverted triangle) and homogeneous model (short dash line) for $b = 0.25$; CFD model (open square) and homogeneous model (dash–dot line) for $b = 0.5$; CFD model (open triangle) and homogeneous model (dash–double dot line) for $b = 0.75$; CFD model (open circle) and homogeneous model (solid line) for $b = 1.0$.

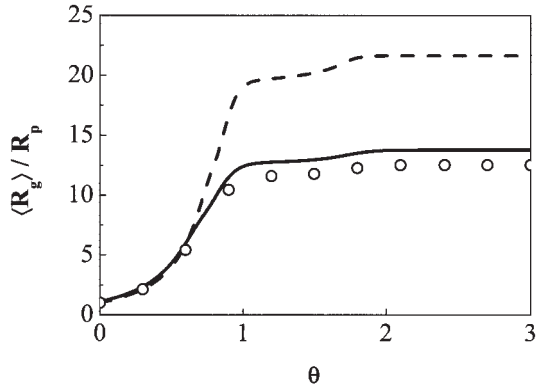

Figure 10. $\langle R_g \rangle / R_p$ as a function of dimensionless time for aggregation efficiency equal to 4/3; CFD model (solid line), lumped model (dash line), and homogeneous model (open circles).

$\bar{G} = 110\ s^{-1}$; $\phi_s = 5.0 \times 10^{-5}$; Taylor–Couette reactor.

agreement and highlights the important limitations of the lumped model.

As mentioned earlier, the aggregation rate prefactor α obtained from the fitting procedure and used in all previous simulations is equal to 0.15. The range of validity of the homogeneous model was further tested by changing the aggregation and breakage rate prefactors. In the case of aggregation we increased the value of the aggregation rate prefactor up to the maximum theoretical value[59] equal to $\alpha_A(\xi, \xi') = 4/3$ and keeping $W = 1.0$ (see Eq. 14). As it is possible to see from Figure 10, the agreement between the CFD and the homogeneous models is worse but still satisfactory.

Another test was done by reducing the value of the breakage rate prefactor to $P_1 = 1.55 \times 10^{10}$, where again we attain very good agreement with the CFD model (see Figure 11). The last test was directed toward establishing a range of validity of the homogeneous model in terms of solids volume fraction ϕ_s. When the solids volume fraction was increased to $\phi_s = 4.0 \times 10^{-4}$, the overall agreement was still good, but some discrep-

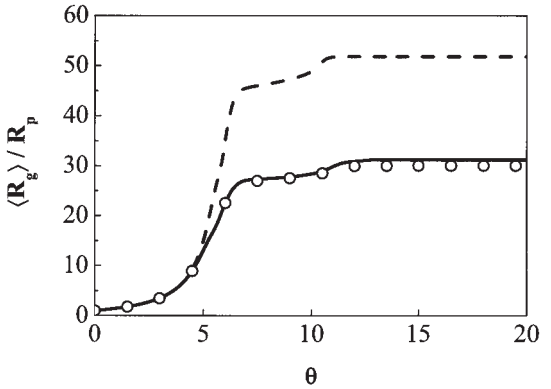

Figure 11. $\langle R_g \rangle / R_p$ as a function of dimensionless time predicted by CFD (solid line), lumped (dash line), and homogeneous (open circles) models with modified breakage kernel, that is, $P_1 = 1.55 \times 10^{10}$.

$\bar{G} = 110\ s^{-1}$; $\phi_s = 5.0 \times 10^{-5}$; Taylor–Couette reactor.

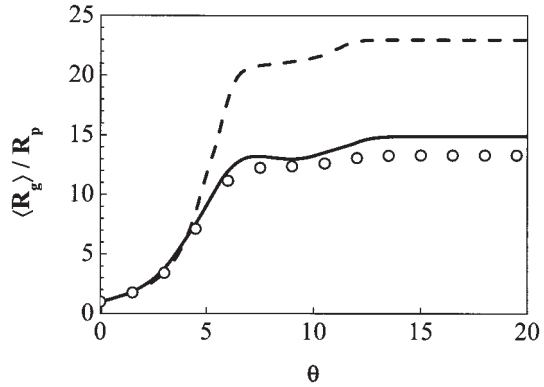

Figure 12. $\langle R_g \rangle / R_p$ as a function of dimensionless time predicted by CFD (solid line), lumped (dash line), and homogeneous (open circles) models.

$\bar{G} = 110\ s^{-1}$; $\phi_s = 4.0 \times 10^{-4}$; Taylor–Couette reactor.

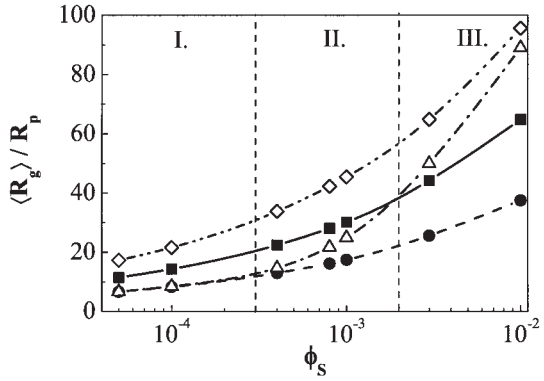

Figure 14. Steady-state $\langle R_g \rangle / R_p$ values as a function of solids volume fraction ϕ_s predicted by CFD (open triangles), lumped (filled squares), instantaneous equilibrium (open diamonds), and homogeneous (filled circles) models.

$\bar{G} = 110\ s^{-1}$; Taylor–Couette reactor.

ancies could be detected (see Figure 12). When the concentration was increased to $\phi_s = 1.0 \times 10^{-3}$, as shown in Figure 12, the agreement was lost and the CFD results were intermediate between those of the homogeneous and the lumped models (see Figure 13).

In Figure 14 the values of the steady-state mean radius of gyration predicted by the CFD, lumped, homogeneous, and instantaneous equilibrium models are shown as a function of solids volume fraction. It is seen that the CFD predictions at low concentration ($\phi_s < 3.0 \times 10^{-4}$) overlap with the homogeneous model predictions, whereas significant differences arise as the solids volume fraction increases. On the other hand, the values calculated by the instantaneous equilibrium model are always larger than those predicted by the CFD model, although the difference decreases as the solids volume fraction increases. It should be noted that the instantaneous equilibrium model has little physical meaning at these high concentrations where aggregation and breakage are characterized by timescales comparable to those of turbulent fluctuations. We should point out that, although breakage rate is not directly dependent on solids volume fraction, it is strongly dependent on the aggregate size. This means that with increasing solids volume fraction steady-state aggregate size increases, resulting in an increase of breakage rate.

From the results in Figure 14 we can conclude that the CFD model, which is computationally very expensive, can be replaced by the homogeneous model at low solids volume fractions (region I). As the solids volume fraction increases (region II), the two models give different results and full CFD coupled with the PBE should be used. For the very dense systems with solids volume fraction $\phi_s > 2.0 \times 10^{-3}$ neither one of the models discussed here is likely to be reliable because of the importance of micromixing as well as the effect of particles on fluid flow. The combination of all these factors results in the most complicated situation (region III), in which multiphase CFD simulation including PBE and micromixing model is required. From the results shown in Figure 14 we also see that the lumped model does not account for the effect of the shear rate distribution and thus tends to underestimate breakage rates and thus overestimate the mean radius of gyration. This is particularly dangerous when solving the inverse problem. Suppose in fact that we estimate kinetic parameters from experimental data using the homogeneous model. Then we ignore the shear rate distribution, which becomes a hidden factor in the estimation process, and therefore the estimated values are valid only as long as the shear rate distribution remains similar. Therefore, if the corresponding estimates of kinetic parameters are used for another vessel with the same average shear rate but different distribution (such as Taylor–Couette vs. stirred tank) the predicted dependency of the CMD on the average shear rate would be incorrect.

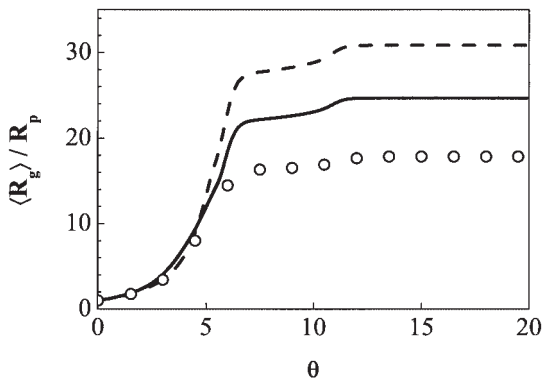

Figure 13. $\langle R_g \rangle / R_p$ as a function of dimensionless time predicted by CFD (solid line), lumped (dash line), and homogeneous (open circles) models.

$\bar{G} = 110\ s^{-1}$; $\phi_s = 1.0 \times 10^{-3}$; Taylor–Couette reactor.

Particle tracking

It is desirable now to generalize the results reported in Figure 14 by introducing suitable criteria for establishing for which conditions the homogeneous model can replace the CFD model. To address this issue some particle-tracking simulations were carried out. Particle tracking was done in FLUENT using multiple injections and a stochastic model for turbulent diffu-

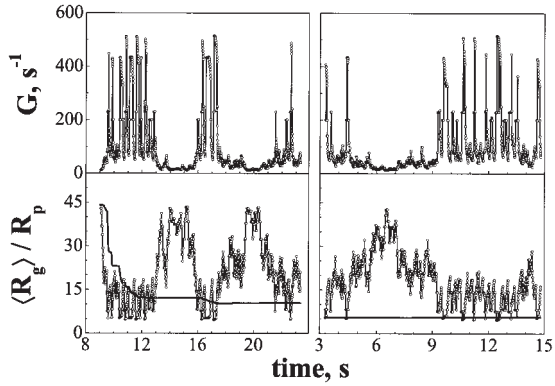

Figure 15. Instantaneous values of shear rate G and corresponding $\langle R_g \rangle / R_p$ values calculated for two different particle trackings (left: particle tracking A; right: particle tracking B), $\bar{G} = 110$ s^{-1} and $\phi_s = 5.0 \times 10^{-5}$.

Thin continuous line with open circles: equilibrium model; thick continuous line: relaxation model.

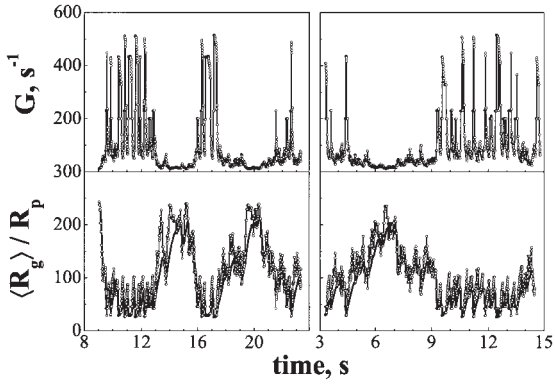

Figure 16. Instantaneous values of shear rate G and corresponding $\langle R_g \rangle / R_p$ values calculated for two different particle trackings (left: particle tracking A; right: particle tracking B), $\bar{G} = 110$ s^{-1} and $\phi_s = 1.0 \times 10^{-3}$.

Thin continuous line with open circles: equilibrium model; thick continuous line: relaxation model.

sion. It is worth noting that if several realizations of the particle tracking are averaged to build the shear rate volume distribution, the result is very similar to that reported in Figure 7, which illustrates the peculiarity of the Taylor–Couette cell, where particles inside each vortex are almost perfectly mixed and experience very similar shear rate histories.

This shear rate history calculated for a given particle can be used to track the changes in the CMD of a population of aggregates moving along with the fluid element containing that particle. The results shown in Figure 15 are for two particles injected at two different locations. The top plots represent the shear rate history for each particle, whereas the bottom plots show the average radius of gyration of the corresponding CMD as a function of time. In particular the thin line with open circles is calculated by assuming that at each change of shear rate the CMD is able to immediately relax to the new steady-state solution (instantaneous equilibrium model), whereas the thick line corresponds to simulating the actual changes in the CMD for the given time during which the particles are subjected to that specific shear rate value (relaxation model). It is seen that in this case, which corresponds to a low solids volume fraction (that is, $\phi_s = 5.0 \times 10^{-5}$), aggregation is rather slow whereas breakage, which is strongly favored at high shear rates, is able to break aggregates down to a very small size. The main conclusion (also confirmed by other particle-tracking experiments not reported here) is that at low solids volume fractions the aggregates are not able to relax to the local value of G and they reach a minimum size that is very close to that predicted by the CFD model. In the case of sufficiently higher values of solids volume fractions, such as $\phi_s = 1.0 \times 10^{-2}$ in Figure 16, the picture is quite different. Aggregation is now much faster, to the extent that the CMD is able to relax to the local value of shear rate following very closely the value of the radius of gyration corresponding to the instantaneous equilibrium value.

This is also confirmed by the contour plots of the mean radius of gyration at the end of the time-dependent simulations (that is, $\theta > 20$) reported in Figures 17 and 18 for two different concentrations, $\phi_s = 5.0 \times 10^{-5}$ and 1.0×10^{-3}, respectively. The contour plot represents a meridian section of the Taylor–Couette reactor, where the boundary line on the left is the outer cylinder and the boundary line on the right is the inner one. It is seen that the gradients in Figure 17 are very small because the time for the CMD to relax to the local value of shear rate is too long compared with the characteristic time of the change in the shear rate experienced by the particles. The situation is very different at higher concentration, as shown in Figure 18, where at steady state persistent gradients are present. It is worth noting that the solutions reported in Figures 17 and 18 are steady-state solutions of Eq. 1. In fact, if at the end of the simulation the time-dependent solver is switched to the steady-state solver, the same solution is obtained.

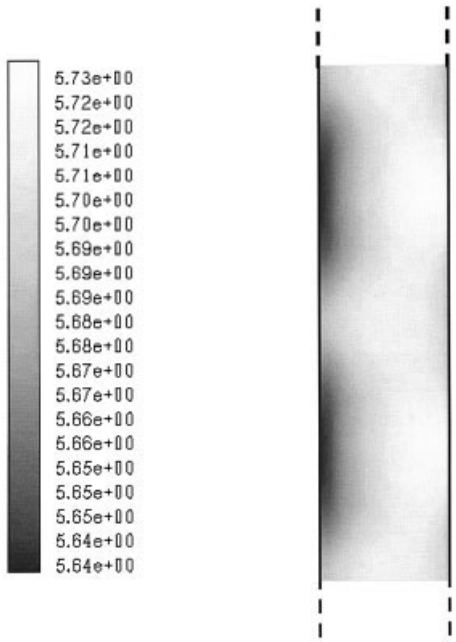

Figure 17. Contour plot of $\langle R_g \rangle / R_p$ at steady-state for $\bar{G}$ = 110 s^{-1} and $\phi_s = 5.0 \times 10^{-5}$.

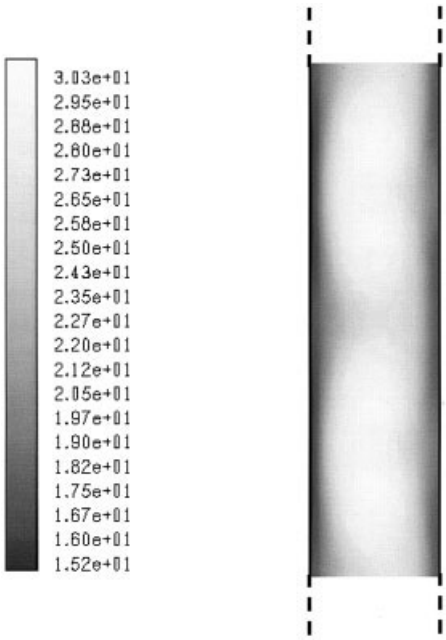

Figure 18. Contour plot of $\langle R_g \rangle / R_p$ at steady-state for $\bar{G} = 110\ s^{-1}$ and $\phi_s = 1.0 \times 10^{-3}$.

To quantitatively identify the characteristic times controlling these processes we now consider the steady-state form of the population balance (see Eq. 1) in dimensionless form, by introducing the following dimensionless quantities

$$N = \frac{n(\xi;\, \mathbf{x},\, t)}{N_t} \qquad X_i = \frac{x_i}{d} \qquad U_i = \frac{\langle u_i \rangle}{d/\tau_M}$$

$$\Gamma_t = \frac{D_t}{d^2/\tau_M} \qquad K^A = \frac{k^A(G;\, \xi,\, \xi')}{k^A(\bar{G};\, \langle \xi \rangle,\, \langle \xi \rangle)} \qquad K^B = \frac{k^B(G;\, \xi)}{k^B(\bar{G};\, \langle \xi \rangle)} \tag{39}$$

where N_t is the volume-averaged total number density of aggregates at steady state, d is a characteristic distance (that is, the annular gap in the Taylor–Couette reactor), τ_M is a characteristic mixing time that will be defined later, and $\langle \xi \rangle$ is the average mass of the aggregates at steady state. By using these quantities Eq. 1 reduces to

$$\begin{aligned}
&\frac{1}{\tau_M}\frac{\partial}{\partial X_i}\left[U_i N(\xi;\, \mathbf{X},\, \theta)\right] - \frac{1}{\tau_M}\frac{\partial}{\partial X_i}\left[\Gamma_t \frac{\partial N(\xi;\, \mathbf{X},\, \theta)}{\partial X_i}\right] \\
&\quad = \frac{1}{2\tau_A}\int_0^{\xi} K^A(G;\, \xi - \xi',\, \xi')\, N(\xi - \xi';\, \mathbf{X},\, \theta)\, N(\xi';\, \mathbf{X},\, \theta)\, d\xi' \\
&\qquad - \frac{1}{\tau_A} N(\xi;\, \mathbf{X},\, \theta) \int_0^{\infty} K^A(G;\, \xi,\, \xi')\, N(\xi';\, \mathbf{X},\, \theta)\, d\xi' \\
&\qquad + \frac{1}{\tau_B}\int_{\xi}^{\infty} K^B(G;\, \xi')\, b(\xi|\xi')\, N(\xi';\, \mathbf{X},\, \theta)\, d\xi' \\
&\qquad - \frac{1}{\tau_B} K^B(G;\, \xi)\, N(\xi;\, \mathbf{X},\, \theta)
\end{aligned} \tag{40}$$

where

$$\tau_A = \frac{1}{k^A(\bar{G};\, \langle \xi \rangle,\, \langle \xi \rangle)\, N_t} \tag{41}$$

is the characteristic time for aggregation (that is, the average time interval between two consecutive aggregation events) and

$$\tau_B = \frac{1}{k^B(\bar{G};\, \langle \xi \rangle)} \tag{42}$$

is the characteristic time for breakage. The left-hand side of Eq. 40 is conservative and describes the role of mixing in smoothing down the gradients generated by the source terms in the right-hand side, which are generally functions of position arising from the space heterogeneity of the shear rate. The rate of dissipation of gradients of the CMD can be quantified by a proper choice of the mixing time τ_M, whereas the rate of change of the CMD can be quantified by the aggregation and breakage characteristic times τ_A and τ_B. It is clear that when τ_M is much smaller than both τ_A and τ_B, mixing is faster than aggregation and breakage and therefore the gradients of the CMD tend to vanish, whereas when τ_A and τ_B are smaller than τ_M the CMD relaxes to the local shear rate value, leaving stable gradients. These two situations correspond to the relaxation and the instantaneous equilibrium models described earlier.

The mixing time can be quantified in several different ways: as the ratio between the annular gap d and the velocity magnitude $|\mathbf{u}|$; or the ratio between the square of the annular gap and the turbulent diffusivity ($\tau_M = d^2/\Gamma_t$); or by the integral scale of turbulence ($\tau_M = k/\varepsilon$), where k is the turbulent kinetic energy.[60] All these definitions lead to a volume-averaged value of τ_M, which for the particular system under examination here, is about 0.1 s. At low concentration, $\phi_s = 5.0 \times 10^{-5}$, τ_A and τ_B have lower bounds of 16 and about 12 s, respectively. On the other hand, increasing the solids volume fraction results in faster aggregation, which leads to larger sizes, which in turn implies faster breakage. Accordingly, at high concentration, $\phi_s = 1.0 \times 10^{-2}$, τ_A and τ_B have lower bounds of 0.015 and 0.021 s, respectively.

In Figure 19 the lower and upper bounds of the characteristic aggregation and breakage timescales, together with the upper and lower bounds of mixing timescales, are shown as a function of the solids volume fraction. These values are obtained

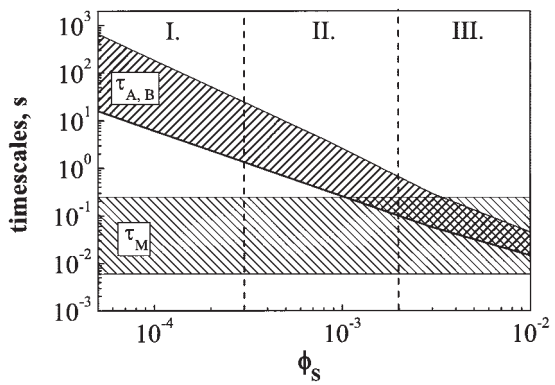

Figure 19. Characteristic times for aggregation, breakage, and mixing as function of solids volume fraction.

using the relations defined above and the solution of the CFD code, which accounts for the heterogeneity of the fluid field. One can see that for dilute systems ($\phi_s < 3 \times 10^{-4}$) the two timescales are well separated and therefore the homogeneous model provides reliable results (region I), whereas at higher concentrations the two timescales are much closer to each other and therefore the CFD model has to be used (region II). For very high concentrations (region III) the instantaneous equilibrium model could be used instead of the full CFD model, although, in most of the practical cases this occurs in a solids concentration range where the effect of the solid phase on the liquid phase[61] and the effect of micromixing are significant.

Conclusions

We compared three different numerical methods—the sectional method, the fixed-pivot method, and the QMOM—to solve population-balance models for aggregation and breakage processes in turbulent flows. We found that, in the case when polynomial kernels are used, such as the power-law breakage kernel, the QMOM approach gives reliable results with two or four nodes, depending on whether only steady-state simulations or also dynamic simulations are considered. To study the effect of spatial heterogeneities on aggregation and breakage, QMOM has been implemented in a CFD code to solve distributed population-balance models. This approach constitutes the full CFD model. We have also introduced several simplified models where the solution of the PBEs is decoupled from the CFD code.

The so-called lumped model, based on the assumption of a uniform shear rate, corresponding to the volume averaged energy dissipation rate, was found to be inappropriate even in dilute conditions. If the lumped model is used to extract information on aggregation and breakage kinetics in a given flow field, one obtains kinetic parameters that are functions of the shape of the shear rate distribution. Such parameters are not exportable to different conditions or devices with different shear rate distributions.

Instead, under conditions where spatial concentration gradients are negligible, the CFD model can be accurately approximated by the homogeneous model. However, the knowledge of the shear rate distribution is crucial. The spatially distributed aggregation and breakage rates need in fact to be properly averaged to achieve correct aggregation and breakage kernels for this model.

We have proposed general criteria, based on mixing, aggregation, and breakage timescales, to establish when the full CFD model can be replaced by the homogeneous model. We illustrate our analysis using a Taylor–Couette reactor. In particular, when aggregation and breakage timescales are much shorter than macromixing timescales, the homogeneous model can be profitably used. When aggregation and breakage timescales are comparable to macromixing timescales, the full CFD model should be used.

Acknowledgments

This work was financially supported by Swiss National Science Foundation (Grant 200020-101724).

Literature Cited

1. Sorensen CM. Light scattering by fractal aggregates: A review. *Aerosol Sci Technol.* 2001;35:648-687.
2. Biggs CA, Lant PA. Activated sludge flocculation: On-line determination of floc size and the effect of shear. *Water Res.* 2000;34:2542-2550.
3. Flesch JC, Spicer PT, Pratsinis SE. Laminar and turbulent shear-induced flocculation of fractal aggregates. *AIChE J.* 2000;45:1114-1124.
4. Kusters KA, Wijers JG, Thoenes D. Aggregation kinetics of small particles in agitated vessels. *Chem Eng Sci.* 1997;52:107-121.
5. Oles V. Shear-induced aggregation and breakup of polystyrene latex particles. *J Colloid Interface Sci.* 1992;154:351-358.
6. Selomulya S, Bushell G, Amal R, Waite TD. Aggregation mechanisms of latex of different particle size in a controlled shear environment. *Langmuir.* 2002;18:1974-1984.
7. Serra T, Colomer J, Casamitjana X. Aggregation and breakage of particles in a shear flow. *J Colloid Interface Sci.* 1997;187:466-473.
8. Serra T, Casamitjana X. Structure of the aggregates during the process of aggregation and breakup under shear flow. *J Colloid Interface Sci.* 1998;206:505-511.
9. Waldner MH, Sefcik J, Soos M, Morbidelli M. Initial growth kinetics of aggregates in turbulent coagulator. *Powder Technol*. 2005; in press.
10. Rahmani NHG, Masliyah JH, Dabros T. Characterization of asphaltenes aggregation and fragmentation in a shear field. *AIChE J.* 2003; 49:1645-1655.
11. Runkana V, Somasundaran P, Kapur PC. Mathematical modeling of polymer-induced flocculation by charge neutralization. *J Colloid Interface Sci.* 2004;270:347-358.
12. Selomulya S, Bushell G, Amal R, Waite TD. Understanding the role of restructuring in flocculation: The application of a population balance model. *Chem Eng Sci.* 2003;58:327-338.
13. Somasundaran P, Runkana V. Modeling flocculation of colloidal mineral suspensions using population balances. *Int J Miner Process.* 2003;72:33-55.
14. Zhang JJ, Li XY. Modeling particle-size distribution dynamics in a flocculation system. *AIChE J.* 2003;49:1870-1882.
15. Kramer TA, Clark MM. Modeling orthokinetic coagulation in spatially varying laminar flow. *J Colloid Interface Sci.* 2000;227:251-261.
16. Ducoste JJ, Prat O. Aggregation of small particles in turbulent liquid flows. Modeling spatial distribution of floc size in turbulent processes using quadrature method of moments and computational fluid dynamics. *Proc. of 2nd Int. Conf. on Population Balance Modeling* Valencia, Spain, May 4–8; 2004:81-84.
17. Hollander ED, Derksen JJ, Bruinsma OSL, van den Akker HEA, van Rosmalen GM. A numerical study on the coupling of hydrodynamics and orthokinetic agglomeration. *Chem Eng Sci.* 2001;56:2531-2541.
18. Marchisio DL, Vigil RD, Fox RO. Implementation of the quadrature method of moments in CFD codes for aggregation-breakage problems. *Chem Eng Sci.* 2003;58:3337-3351.
19. Vanni M, Sommerfeld M. Aggregation of small particles in turbulent liquid flows. Proc of the Third International Symposium on Engineering Turbulence Modelling and Measurements, Heraklion-Crete, Greece, May 27–29; 1996:891-900.
20. Ducoste JJ, Clark MM. The influence of tank size and impeller geometry on turbulent flocculation: I. Experiment. *Environ Eng Sci.* 1998;15:215-224.
21. Hanson AT, Cleasby JL. The effects of temperature on turbulent flocculation: Fluid dynamics and chemistry. *J Am Water Works Assoc.* 1990;82:56-73.
22. Oldshue JY, Mady OB. Flocculation performance of mixing impellers. *Chem Eng Prog.* 1978;74:103-108.
23. Ramkrishna D. *Population Balances: Theory and Applications to Particulate Systems in Engineering*. New York, NY: Academic Press; 2000.
24. Baldyga J, Orciuch W. Some hydrodynamic aspects of precipitation. *Powder Technol:* 2001;121:9-19.
25. Saffman PG, Turner JS. On the collision drops in turbulent clouds. *J Fluid Mech.* 1956;1:16-31.
26. Elimelech M, Gregory J, Jia X, Wiliams RA. *Particle Deposition and Aggregation, Measurement, Modelling and Simulation*. London, UK: Butterworth-Heinemann; 1995.
27. Meakin P. Fractal aggregates. *Adv Colloid Interface Sci.* 1988;28:249-331.
28. Sandükhler P, Sefcik J, Lattuada M, Wu H, Morbidelli M. Modeling structure effects on aggregation kinetics in colloidal dispersions. *AIChE J.* 2003;49:1542-1555.
29. Vanni M. Creeping flow over spherical permeable aggregates. *Chem Eng Sci.* 2000;55:685-698.
30. Lattuada M, Wu H, Morbidelli M. Hydrodynamic radius of fractal clusters. *J Colloid Interface Sci.* 2003;268:96-105.
31. Lattuada M, Wu H, Morbidelli M. A simple model for the structure of fractal aggregates. *J Colloid Interface Sci.* 2003;268:106-120.

32. Sorensen CM, Roberts GC. The prefactor of fractal aggregates. *J Colloid Interface Sci.* 1997;186:447-452.
33. Vanni M, Baldi G. Coagulation efficiency of colloidal particles in shear flow. *Adv Colloid Interface Sci.* 2002;97:151-177.
34. Hulburt HM, Katz S. Some problems in particle technology. *Chem Eng Sci.* 1964;19:555-574.
35. Diemer RB, Olson JH. A moment methodology for coagulation and breakage problems: Part 2—Moment models and distribution reconstruction. *Chem Eng Sci.* 2002;57:2211-2228.
36. McGraw R. Description of aerosol dynamics by the quadrature method of moments. *Aerosol Sci Technol.* 1997;27:255-267.
37. Marchisio DL, Vigil RD, Fox RO. Quadrature method of moments for aggregation-breakage processes. *J Colloid Interface Sci.* 2003;258: 322-334.
38. Marchisio DL, Pikturna JT, Fox RO, Vigil RD, Barresi AA. Quadrature method of moments for population balances. *AIChE J.* 2003;49: 1266-1276.
39. Fan R, Marchisio DL, Fox RO. Application of the direct quadrature method of moments to polydisperse gas–solid fluidized beds. *Powder Technol.* 2004;139:7-20.
40. McGraw R, Wright DL. Chemically-resolved aerosol dynamics for internal mixtures by the quadrature method of moments. *J Aerosol Sci.* 2003;34:189-209.
41. Marchisio DL, Fox RO. Solution of population balance equations using the direct quadrature method of moments. *J Aerosol Sci.* 2005; 36:43-73.
42. Rosner DE, Pyykonen JJ. Bivariate moment simulation of coagulation and sintering nanoparticles in flames. *AIChE J.* 2002;48:476-491.
43. Wright DL, McGraw R, Rosner DE. Bivariate extension of the quadrature method of moments for modeling simultaneous coagulation and sintering of particle populations. *J Colloid Interface Sci.* 2001;236: 242-251.
44. Zucca A, Marchisio DL, Barresi AA, Fox RO. Implementation of the population balance equation in CFD codes for modelling soot formation in turbulent flames. *Chem Eng Sci*. 2004;00:000-000.
45. Barrett JC, Webb NA. A comparison of some approximate methods for solving the aerosol general dynamic equation. *J Aerosol Sci.* 1998;29:31-39.
46. Dette H, Studden WJ. *The Theory of Canonical Moments with Applications in Statistics, Probability, and Analysis*. New York, NY: Wiley; 1997.
47. Press WH, Teukolsky SA, Vetterling WT, Flannery BP. *Numerical Recipes in Fortran 77: The Art of Scientific Computing*. Cambridge, UK: Cambridge Univ. Press; 1992.
48. Gordon RG. Error bounds in equilibrium statistical mechanics. *J Math Phys.* 1968;9:655-667.
49. Vanni M. Approximate population balance equation for aggregation-breakage processes. *J Colloid Interface Sci.* 2000;221:143-160.
50. Batterham RJ, Hall JS, Barton G. Pelletizing kinetics and simulation of full scale balling circuits. Proc of the 3rd international Symposium on Agglomeration, Nurnberg, W. Germany; 1981:A136.
51. Hounslow MJ, Ryall RL, Marshall VR. A discretized population balance for nucleation, growth, and aggregation. *AIChE J.* 1988;34: 1821-1832.
52. Kumar S, Ramkrishna D. On the solution of population balance equations by discretization—I. A fixed pivot technique. *Chem Eng Sci.* 1996;51:1311-1332.
53. Kataoka K. Taylor vortices and instabilities in circular Couette flows. In: Cheremisinoff NP, ed. *Encyclopedia of Fluid Mechanics*. Vol. 1. Houston, TX: Gulf Publishing, 1986:237-273.
54. Marchisio DL, Barresi AA. CFD simulation of mixing and reaction: The relevance of the micromixing model. *Chem Eng Sci.* 2003;58:579-3587.
55. Lattuada M, Wu H, Sandkühler P, Sefcik J, Morbidelli M. Modelling of aggregation kinetics of colloidal systems and its validation by light scattering measurements. *Chem Eng Sci.* 2004;59:1783-1798.
56. Sandkühler P, Sefcik J, Morbidelli M. Kinetics of aggregation and gel formation in concentrated polystyrene colloids. *J Phys Chem B.* 2004; 108:20105-20121.
57. Zimm BH. Apparatus and methods for measurement and interpretation of the angular variation of light-scattering: Preliminary results on polystyrene solutions. *J Chem Phys.* 1948;16:1099-1123.
58. Wang L, Marchisio DL, Vigil RD, Fox RO. CFD simulation of aggregation and breakage processes in laminar Taylor–Couette flow. *J Colloid Interface Sci.* 2005;282:380396.
59. Smoluchowski MZ. Versuch einer mathematischen Theorie der koagulationskinetik Colloider Losunger. *Z Phys Chem.* 1917;92:129-142.
60. Fox RO. *Computational Models for Turbulent Reacting Flows*. Cambridge, UK: Cambridge Univ. Press; 2003.
61. Barthelmes G, Pratsinis SE, Buggisch H. Particle size distribution and viscosity of suspensions undergoing shear-induced coagulation and fragmentation. *Chem Eng Sci.* 2003;58:2893-2902.

Appendix

The *product-difference* (PD) algorithm is used here to find weights (w_i) and abscissas (L_i) from the moments of the distribution. The first step is the construction of a matrix **P** with components $P_{i,j}$ starting from the moments. The components in the first column of **P** are

$$P_{i,1} = \delta_{i1} \qquad i \in 1, \ldots, 2N+1 \tag{A1}$$

where δ_{i1} is the Kronecker delta. The components in the second column of **P** are

$$P_{i,2} = (-1)^{i-1} m_{i-1} \qquad i \in 1, \ldots, 2N \tag{A2}$$

Because the final weights can be corrected by multiplying by the true m_0, the calculations can be done assuming a normalized distribution (that is, $m_0 = 1$). The remaining components are found from the PD algorithm

$$P_{i,j} = P_{1,j-1}P_{i+1,j-2} - P_{1,j-2}P_{i+1,j-1} \qquad j \in 3, \ldots, 2N+1 \quad \text{and} \quad i \in 1, \ldots, 2N+2-j \tag{A3}$$

The coefficients of the continued fraction (α_i) are generated by setting the first element equal to zero ($\alpha_1 = 0$) and computing the others according to the following recursive relationship

$$\alpha_i = \frac{P_{1,i+1}}{P_{1,i}P_{1,i-1}} \qquad i \in 2, \ldots, 2N \tag{A4}$$

A symmetric tridiagonal matrix is obtained from sums and products of α_i

$$a_i = \alpha_{2i} + \alpha_{2i-1} \qquad i \in 1, \ldots, N \tag{A5}$$

and

$$b_i = -\sqrt{\alpha_{2i+1}\alpha_{2i}} \qquad i \in 1, \ldots, N-1 \tag{A6}$$

where a_i and b_i are, respectively, the diagonal and the codiagonal of the Jacobi matrix. Once the tridiagonal matrix is determined, generation of the weights and abscissas is done by finding its eigenvalues and eigenvectors. In fact, the eigenvalues are the abscissas and the weights can be found as follows

$$w_j = m_0 v_{j1}^2 \tag{A7}$$

where v_{j1} is the first component of the jth eigenvector $\mathbf{v}_j$.

Manuscript received Nov. 29, 2004, and revision received May 17, 2005.